AUCTORES
Globalize your Research

Clinical Research and Clinical Trials

Delia Teresa Sponza *

Open Access

Research Article

Photocatalytic H_2 Production from Hydrazine Monohydrate ($N_2H_4.H_2O$) using Ni–W–O Nanocomposite

Delia Teresa Sponza *, Rukiye Öztekin [1]

Dokuz Eylül University, Engineering Faculty, Department of Environmental Engineering, Tınaztepe Campus, 35160 Buca/Izmir, Turkey.

***Corresponding Author:** Delia Teresa Sponza, Dokuz Eylül University, Engineering Faculty, Department of Environmental Engineering, Tınaztepe Campus, 35160 Buca/Izmir, Turkey.

Received date: 16 August 2023; Accepted date: 15 October 2023; Published date: 04 December 2023

Citation: Delia T. Sponza, Rukiye Öztekin, (2023), Photocatalytic H_2 Production from Hydrazine Monohydrate ($N_2H_4.H_2O$) using Ni–W–O Nanocomposite, *Clinical Research and Clinical Trials*, 8(2); **DOI:10.31579/2693-4779/158**

Abstract:

In this study, H_2(g) was produced from hydrazine monohydrate using Ni–W–O nanocomposite. The XRD pattern of the synthesized hydrothermal of Ni–W–O nanocomposite samples exhibited some features of that of $NiWO_4$ with poorly crystallized groups. FTIR spectra of the nanocomposite showed an intense peak at 822 cm^{-1} corresponding to the stretching vibrations of O–W–O. TEM analysis indicated the reduction of the small $NiWO_4$ crystallites during production process. In the EDS analysis Ni and W elemental distributions was detected. XPS results shows the presence of Ni (II) and W(VI) at high-temperature annealing. For maximum photodegradation of hydrazine monohydrate ($N_2H_4.H_2O$) to H_2(g) (2.670 l) the conditions were as follows: Ni–W–O nanocomposite concentration of 2 mg/l with a Ni/W/O ratio of 0.8/0.5/0.2, 80 min irradiation time, a ligth power of 90 W/m^2, a temperature of 60ºC and a pH of 8.0.

Keywords: hydrazine monohydrate ($n_2h_4.h_2o$); hydrogen [h_2(g)] production; ni–w–o nanocomposite; photocatalytic degradation

Introduction:

Hydrogen (H_2) is expected to play an essential role as an energy carrier in the future clean energy economy based on renewable energy resources. However, the widespread utilization of hydrogen is hampered by the technical difficulty involved in hydrogen storage and delivery [1]. The materials capable of reversible dehydrogenation have long been sought as possible candidates for high-capacity hydrogen storage [2]. However, none of the existing materials met the requirements for hydrogen capacity (over 6 wt%), kinetics, and operation temperature. Recently, chemical hydrogen storage involving hydrolysis or thermolysis of hydrogen-rich materials and spent-fuel regeneration has emerged as a competitive alternative to a high-pressure hydrogen cylinder for vehicular and portable applications [3]. Among the hydrogen-rich materials of interest, hydrazine monohydrate ($N_2H_4.H_2O$) is an appealing candidate thanks to its favorable combination of low cost, high hydrogen capacity (8.0 wt%), and good stability at ambient temperatures [4]. In particular, the decomposition reactions of N_2H_4 yield only gaseous products, which is highly beneficial for the design and practical application of H_2-source systems. A series of multicyclic bis(hydrazine) and bis(diazenium) compounds connected by relatively rigid hydrocarbon frameworks were prepared for the study of intramolecular electron transfer. The thermodynamics of electron removal of these compounds was investigated by cyclic voltammetry. The difference between the first and second oxidation potentials for the 4 sigma-bonded species was found to be larger for the bis(hydrazyl) radical systems than for the bis(hydrazines) by ca. 0.2 V (4.6 kcal/mol). This indicates a greater degree of interaction between the two nitrogen moieties for the hydrazyl systems, which is consistent with a greater degree of electronic coupling (H {rm AB}) in these systems [5]. The development of $N_2H_4.H_2O$ as a chemical hydrogen storage material requires highly active and selective catalysts for promoting hydrogen production, and meanwhile suppressing the formation of NH_3. In the past decades, a number of transition metals/alloys have been investigated in terms of catalytic properties toward $N_2H_4.H_2O$ decomposition [6]. It was found that alloying is a highly effective approach for boosting the catalytic performance toward HP from $N_2H_4.H_2O$. The alloying aspect could be understood from two complementary effects: the geometric and electronic modifications of the catalyst surface [6-15]. The bimetallic alloys composed of a combination of precious metals (like Pt and Ir) and nonprecious metals (like Ni, Co, and Fe) generally exhibited favorable performance in both activity and H_2(g) selectivity [16-20]. In contrast, the catalytic activity of the noble-metal-free alloys is typically inferior. For instance, the reaction rates of $N_2H_4.H_2O$ decomposition over the representative Ni-based catalysts, such as $NiCu/CeO_2$, NiFe/W. CeO_2, $NiCo/NiO–CoO_x$, and NiMo/NiMoO, were 1 or 2 orders of magnitude lower than those of the NiPt and CoPt catalysts [21-27]. Currently, the less favorable modification effects of non-precious metals compared to noble metals are still poorly understood, but from the perspectives of the cost reduction and growth potential, non-precious-metal catalysts represent an important direction for future research of the $N_2H_4.H_2O$-based HP technology. In general, activity improvement of non-

precious-metal catalysts can be pursued via composition/phase tuning and structure optimization.

Therefore, in this study, H_2(g) production from $N_2H_4.H_2O$ photodecomposition was studied using Ni−W−O-derived nanocatalyst. Operational conditions such as temperature (20, 30, 40, 50, 60, 70, 80 , 90, 100 and 110°C), nanocomposite concentration (0.5, 1.0, 1.5, 2.0, 2.5, 3.0, 3.5 and 4 mg/l), illuminating time (20, 30, 40, 50, 60, 70 , 80 and 120 min), ligth power (20, 30, 40, 50, 60, 70, 80, 90, 100 and 110 W/m^2), pH (4.0, 7.0, 8.0, 9.0, 10.0, 11.0 and 12.0) and Ni/W/O ratios (0.2 / 0.5 / 0.8, 0.5 / 0.8 / 0.2 and 0.8 / 0.5 / 0.2) in the Ni-W-O nanocomposite influencing the H_2(g) production was examined. The physicochemical properties of the Ni−W−O-nanocatalyst produced under laboratory conditions was investigated with X-ray diffraction (XRD), transmission electron microscopy (TEM), Fourier transform infrared spectroscopy (FTIR) and X-ray photoelectron spectroscopy (XPS).

Materials and Methods

1.1. Ni-W-O nanocomposite preparation

Firstly, 2.2 mmol of $Na_2WO_4.2H_2O$ was dissolved into 25 ml of DI water, then 1 g of $NiCl_2.6H_2O$ was added to the aqueous solution. The mixture was stirred for 30 min. The obtained mixture was transferred to an autoclave and kept at 180°C for 4 h. The sample was collected after cooling to ambient temperature and was sequentially washed with deionized water and C_2H_5OH and then dried under vakuum at 80°C for 1 h. The samples was annealed at different temperatures (350, 400, and 600 °C) for H_2(g) production during 100 min.

1.2. Physicochemical properties of Ni-W-O nanocomposite

The structure of the Ni-W-O nanocomposite were characterized by X-ray diffraction (XRD, 2000 using Cu Kα monochromatized radiation), transmission electron microscopy (TEM, JEOL-2100F), Fourier transform infrared spectroscopy (FTIR, Nicolet IS10), Raman spectroscopy (Thermo Scientific DXR with an excitation wavelength of 532 nm), and X-ray photoelectron spectroscopy (XPS, Thermo Scientific using an Al Kα X-ray source). In the XPS studies, carbon was used for calibration of the binding energy scale.

1.3. $N_2H_4.H_2O$ measurement

Hydrazine was measured by ultraviolet–visible spectroscopy at a wave lentgh of 560 nm (UV–vis, 220).

1.4. Photocatalytic decomposition of hydrazine to H_2(g)

$N_2H_4.H_2O$ solution containing the Ni-W-O nanocomposite catalyst and an alkaline aqueous solution was preheated at the desired temperature under magnetic stirring. The generated gaseous products passed through a 1.0 M hydrochloric acid solution to absorb ammonia, if any, and then were measured by the water-displacement method using an electronic balance with a precision of ±0.01 g. In the test of the catalytic decomposition properties of concentrated $N_2H_4.H_2O$ solution, an online mass flowmeter equipped with a silica drier was used to monitor the volume of the gaseous products. The reaction rate was evaluated at a reactant conversion of 50%, assuming all the Ni atoms take part in the catalytic reaction. The H_2(g) was measured with a Dragger H_2 gas meter.

Results and Discussions

1.5. Effect of Ni-W-O nanocatalyst concentration on H2(g) production efficiency from Photo catalytic Performance for H_2(g) production from $N_2H_4.H_2O$

The concentrations of Ni-W-O nanocatalyst was increased from 0.5 mg/l up to 4 mg/l. The maximum H_2(g) production was ontained with 2 mg/l Ni-W-O concentration as 2.670 l (**Table 1**). The increase of nanocatalyst concentration to 3 and 4 mg/l did not affect the H_2(g) production.

Ni-W-O nanocatalyst concentration (mg/l)	H_2(g) production (l)
0.5	0.800
1	1.000
1.5	1.870
2.0	2.670
2.5	2.300
3.0	2.200
3.5	2.000
4.0	2.000

Table 1. Effect of increasing Ni-W-O nanocatalyst concentration on H_2(g) production efficiency

1.6. Effect of Nİ/ W/ O ratios in the Ni-W-O nanocomposite on H_2(g) production efficiency from $N_2H_4.H_2O$

Catalytic properties toward $N_2H_4.H_2O$ photodegradation were studied on the Ni–W–O derived nanocomposite catalysts. According to control experiments, changing the molar ratio of Ni/W precursors caused a variation of catalytic properties toward $N_2H_4.H_2O$ decomposition, and the optimal Ni/W precursors molar ratio was determined. Therefore, the Ni/W/O ratios was adjusted to 0.2 / 0.5 / 0.8, to 0.5 / 0.8 / 0.2 and to 0.8 / 0.5 / 0.2 in the 2 mg/l Ni-W-O nanocomposite (**Table 2**). Among these ratios the maximum H_2(g) production was detected with a Ni/W/O ratio of 0.8/ 0.5/ 0.2.

Ni / W / O ratios	H_2(g) production (l)
0.2 / 0.5 / 0.8	1.450
0.5 / 0.8 / 0.2	1.600
0.8 / 0.5 / 0.2	2.765

Table 2. Effect of Ni-W-O ratios in the Ni-W-O nanocatalyst on H_2(g) production efficiency

1.7. Effect of illumination time on H_2(g) production efficiency from $N_2H_4.H_2O$

As shown in **Table 3**, the cumulative H_2(g) production was linearly correlated with illumination time. As the time increased from 20 min up to 80 min the H_2(g) production increased from 2 l up to 2.5 l. Furher increase of time did not affect the H_2(g) production both under solar and visible light irradiation. This behavior is valid in the presence of 2 mg/l Ni-W-O nanocomposite with a Ni / W / O ratio of 0.8 / 0.5 / 0.2.

Illumination time (min)	H_2(g) production (l)
20	0.800
30	1.000
40	1.870
50	2.000
60	2.300
70	2.500
80	2.670
120	2.000

Table 3. Effect of illumination time on H_2(g) production efficiency

1.8. Effect of ligth intensity on H_2(g) production efficiency from $N_2H_4.H_2O$

The efficiency of photocatalytic water splitting can be improved by increasing light intensity with energies more than the activation threshold. The variation of reaction rate as a function of wavelength comes after the adsorption spectrum of the catalyst with a threshold corresponding to the band energy. In this stuy the H_2(g) production increased from 1 l up to 2.760 l when the UV ligth intensity was increased from 30 W/ m^2 up to 90 W/m^2 (**Table 4**). Further increase of UV power did not affect the H_2(g) production. It was recorded that the photocatalytic hydrogen production using Ni-W-O showed 50% improved photoactivity by increasing light light intensity was increased.

Ligth intensity (W/m^2)	H_2(g) production (l)
20	0.800
30	1.000
40	1.870
50	2.000
60	2.300
70	2.500
80	2.600
90	2.760
100	2.000
110	2.000

Table 4. Effect of ligth intensity on H_2(g) production efficiency

1.9. Effect of iIncreasing temperature on H_2(g) production efficiency from $N_2H_4.H_2O$

Thermodynamically, temperature cannot induce the photocatalysis activity, since it did not contribute toward the generation of electrons and holes. However, temperature plays a role to enhance desorption of products from the surface of catalyst to increase the photocatalytic activity. The temperature speeds up the reaction rate. The temperature applied differs for different catalyst. Therefore, this factor could quickly be adjusted to increase the photocatalytic activity. In this study as the temperature was increased from 20ºC to 60ºC the H_2(g) production elevated from 0.600 l up to 2.700 l (**Table 5**). Reduce temperature gives negative effect by slowing the H_2(g) production rate as desorption of the products limits the reaction, since it is slower the adsorption of the reactants. High temperature provides higher electron transfers in valance band to higher energy levels. Thus, it facilitates the electrone hole formation that could be utilized in initiating oxidation and reduction reactions, respectively, and helps the reaction to compete more effectively with charge carries recombination. It was reported that H_2(g) evolution increased with temperature up to 70ºC. Further increasing the temperature, however, seems to deteriorate the reaction rate. It was reported that the catalytic properties of these nanocomposite from the aspects of investigating the intrinsic catalytic properties, the number of active sites and metal–support interactions lpwered at very high temperatures.

Temperature (ºC)	H_2(g) production (l)
20	0.800
30	1.000
40	1.870
50	2.000
60	2.700
70	2.500
80	2.600
90	2.000
100	2.000
110	2.000

Table 5. Effect of increasing temperature on H_2(g) production efficiency

1.10. Effect of pH on $H_2(g)$ production efficiency from $N_2H_4.H_2O$

It can be regarded that the production of $H_2(g)$ from water splitting is dependent upon the proton concentration, which is the pH of the solution, since proton reduction by the photogenerated electron is generated throughout water splitting. This specific aspect is particularly importance in the case of photo reforming as the presence of a sacrificial organic species. In this stuy the maximum $H_2(g)$ generation was detected at a pH of 8.0 (**Table 6**). Acidic and basic conditions decrease the $H_2(g)$ production. It was reported that Ni-W-O catalyst for $H_2(g)$ evolution depends on the pH of the mixture while the optimum pH is close to the zero-point charge. At acidic pH, more Hþ ions are adsorbed on the photo catalyst, so the possibility of the reduction of Hþ to H2 by e^{-1} will not increased. It was reported that in the photocatalytic reaction in low basic system gives more advantages to enhance $H_2(g)$ evolution.

pH	$H_2(g)$ production (l)
4	0.800
5	1.000
7	1.870
8	2.700
9	2.340
10	2000
11	1.000
12	0.400

Table 6. Effect of pH on $H_2(g)$ production efficiency

1.11. Effect of Oxygen on H2(g) production efficiency from $N_2H_4.H_2O$

The metal oxide can be introduced to effect oxygen vacancies by catalyst synthesis, reduction and doping. For Ni-W-O nanocomposite the oxygen vacancies are existed along with Ni-W-O. When the oxygen vacancies concentration is higher, more ions are produced, thus causes a defect state, surface disorder and associate oxygen vacancies. Due to missing oxygen atom, the oxygen vacancies defect can trap and prolong the life of electrons. Whereas, the regular lattice of the oxygen atom was taken by electrons and local state was formed by oxygen vacancies in the Ni-W-O nanocatalyst. Then, the valens band holes of Ni-W-O were generated and the electrons excited to the conduction bant of the nanocomposite. As a result the electroneholes recombination enhanced the $H_2(g)$ production. In order to detect the effects of $O_2(g)$ concentration on $H_2(g)$ production via 2 mg/l Ni-W-O nanocomposite the dissolved oxygen concentration was increased from 0.5 mg/l up to 4 mg/l. The maximum $H_2(g)$ yields was tetected at 1.8 mg/l dissolved oxygen concentration (2.700 l)(**Table 7**).

Dissolved oxygen concentration (mg/l)	$H_2(g)$ production (l)
0	0.800
0.5	1.000
1.0	1.870
1.8	2.700
2.0	2.040
2.5	2.000
3.0	1.000
4.0	0.400

Table 7. Effect of dissolved oxygen on $H_2(g)$ production efficiency

1.12.Physicochemical properties of Ni-W-O nanocomposite

1.12.1. XRD results versus increasing temperatures

The XRD pattern of the as-synthesized hydrothermal sample (**Figure 1**) resembles some features of that of $NiWO_4$ but with significant peak broadening and diffuse scattering, indicating the formation of a poorly crystallized product. Further annealing this sample at elevated temperature (over 400°C) in air could help remove possible solvent residue, improve its crystallinity, promote crystallite growth, and result in a well-defined XRD pattern consistent with that of $NiWO_4$ (JCPDS 15–0755). Because of the poor crystallinity nature of the as-synthesized hydrothermal sample, its phase assignment was further corroborated by the spectroscopic analyses. Reductive annealing the hydrothermal sample at various temperatures resulted in the formation of nanocomposite catalysts with varied phase compositions and structures. As shown in **Figure 1**, the 350°C-reduced sample showed a similar XRD pattern to that of the hydrothermal sample but with a new peak appearing at $2\theta = 43.68°$, matching well with the (111) peak of the $Ni_{17}W_3$ phase (JCPDS 65–4828). Upon increasing the annealing temperature to 400°C, this peak becomes intensified with a low-angle shift by 0.2°, which corresponds well to the (211) peak of the Ni_4W phase (JCPDS 65–2673). Meanwhile, the diffraction peaks from the hydrothermal sample completely disappeared and were replaced by the characteristic peaks from the WO_2 phase (JCPDS 32–1393). With further elevation of the annealing temperature to 600°C, WO_2 was reduced to metal W (JCPDS 04–0806) but with the Ni_4W phase still preserved.

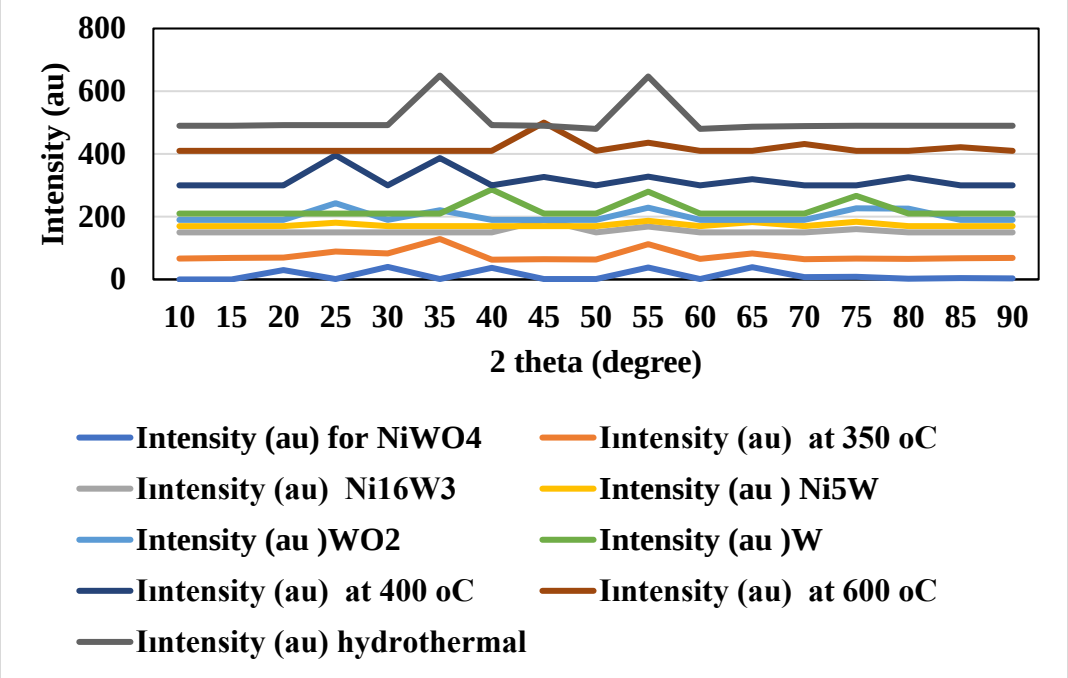

Figure 1. XRD analysis results

1.12.2. FTIR spectra of Ni-W-O nanocomposite

FTIR spectra of the hydrothermal sample exhibited an intense peak at 822 cm^{-1} corresponding to the stretching vibrations of Ni–W–O.

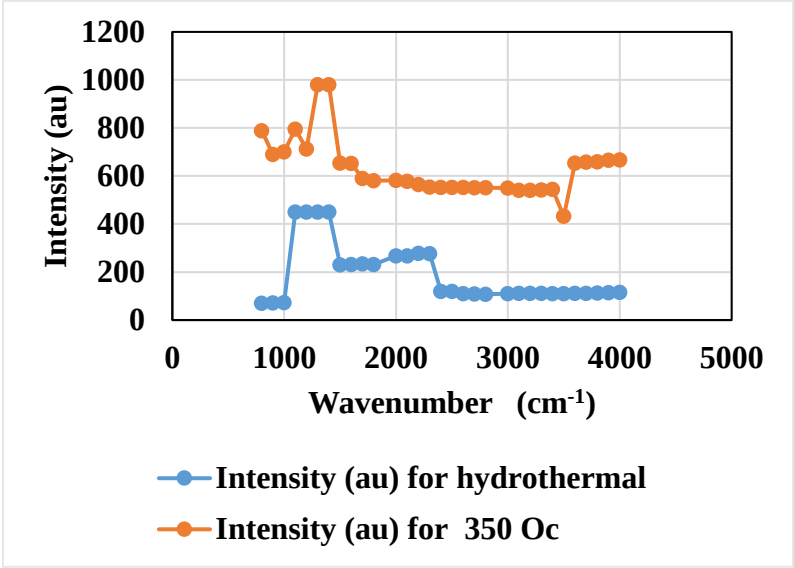

Figure 2: FTIR spectra results

1.12.3. Raman spectra of Ni-W-O nanocomposite

The Raman spectrum clearly showed a strong band at 883 cm^{-1}, which should be ascribed to the stretching vibrational mode of terminal W=O bonds, consistent with the featured assembly of WO_6 octahedra in the $NiWO_4$ structure (**Figure 3**). IR bands at around 1650 and 3400 cm^{-1} in **Figure 3** should be assigned to the OH bending and stretching vibrations of the adsorbed water molecules. The phase assignments of the 400- and 600°C-reduced samples were further supported by the Raman spectra (data not shown).

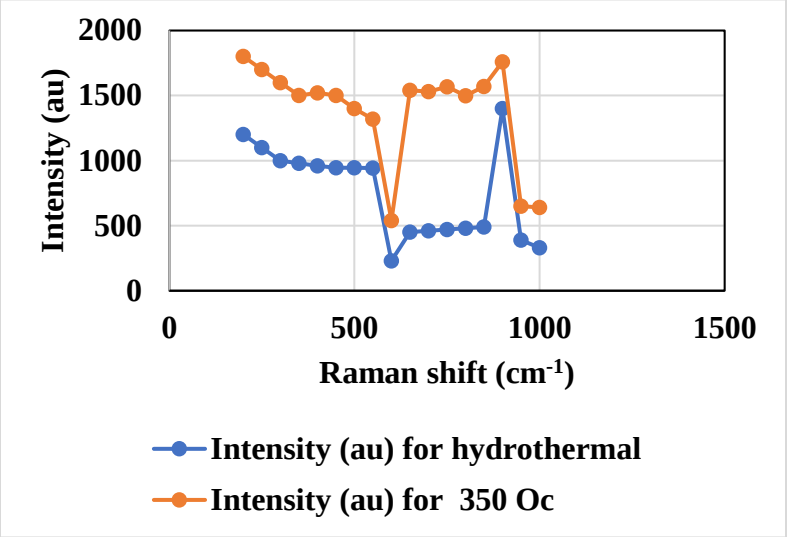

Figure 3: Raman Spectra results

1.12.4. TEM results of spectra of Ni-W-O nanocomposite

Phase structure evolution of the hydrothermal samples upon reductive annealing was further investigated by operating TEM in high-resolution and selected-area electron diffraction (SAED) modes. As shown in **Figure 4a, 4b and 4c**, the SAED patterns discern the evolutionary reduction of the small $NiWO_4$ crystallites in the hydrothermal sample during the reductive annealing process, from the initial precipitation of $Ni_{17}W3$ to the concurrent formation of Ni_4W and WO_2, and further to the metallic Ni_4W and W phases. The high-resolution TEM images reveal the microstructure and phase constitution of the reduced samples. In the 350 °C-reduced sample, the lattice fringes with interplanar distances of 0.207 and 0.245 nm could be assigned to the (111) plane of $Ni_{17}W_3$ and the (002) plane of $NiWO_4$, respectively (**Figure 4d**). Similarly, the characteristic d-spacings from the crystalline Ni_4W and WO_2 nanoparticles were identified in the 400°C-reduced sample (**Figure 4e and 4f**).

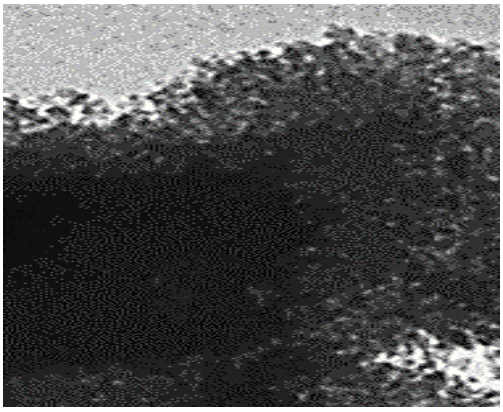

(a)

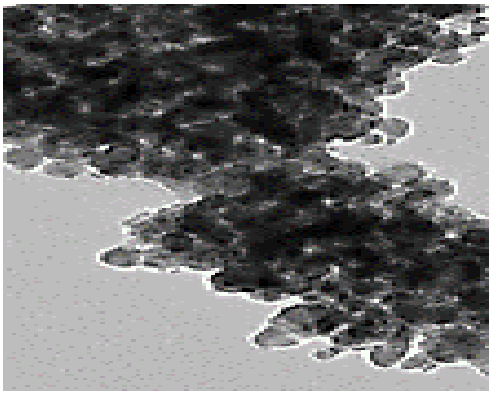

(b)

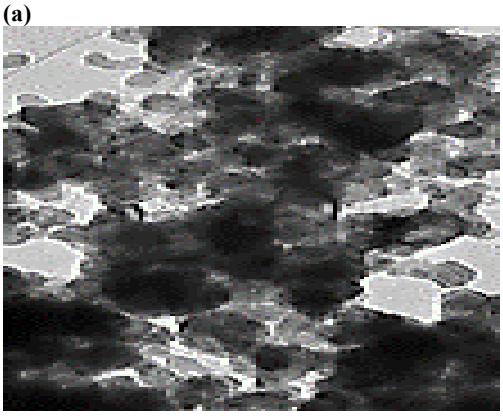

(c)

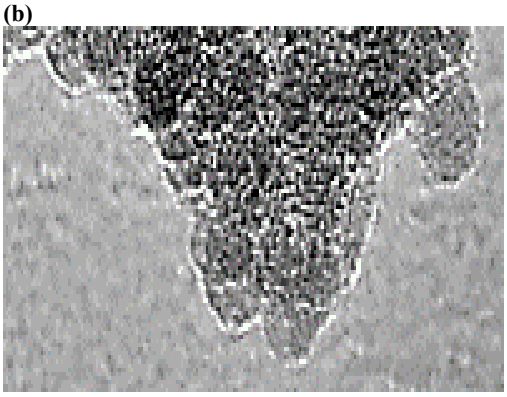

(d)

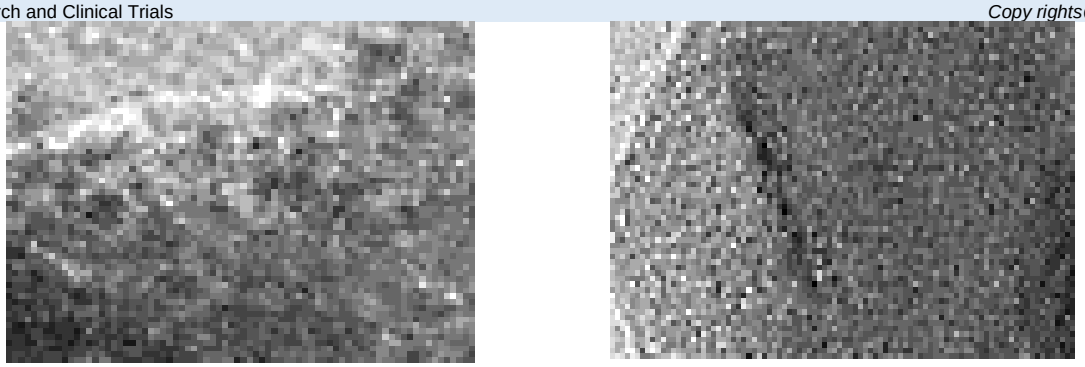

(e) (f)

Figure 4: TEM analysis results (TEM images size: 200 nm).

1.12.5. EDS results of of Ni-W-O nanocomposite

In an effort to determine how the Ni–W alloy phases distribute on the W containing substrates, we examined the reduced samples by high-angle annular dark-field scanning transmission electron microscopy in combination with energy X-ray dispersive spectroscopy (EDS) analysis. The Ni and W elemental distributions gradually change from the atomic dispersion to the segregated nanoclusters with increasing annealing temperature. For the 400°C-reduced sample, the segregation of Ni and W elements became detectable because of the formation of the distinct Ni_4W and WO_2 phases. Further increasing the annealing temperature to 600°C resulted in aggravated segregation Ni and W, owing to the formation of W and the particle growth and aggregation of Ni_4W. A close examination of the samples by EDS line-scanning profile analysis (**Figure 5a, 5b and 5c**) suggested that the size of the Ni_4W nanoparticles increased from around 15 to 30 nm upon elevation of the annealing temperature from 400 to 600°C.

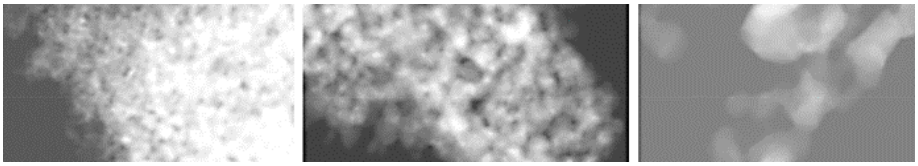

(a) (b) (c)

Figure 5: EDS analysis results (EDS images size: 200 nm).

1.12.6. XPS results of Ni-W-O nanocomposite

The chemical states of the constituent elements in the hydrothermal and reduced samples were also examined using the surface-sensitive XPS. As presented in **Figure 6**, the hydrothermal sample exhibited only Ni(II) and W(VI) signals. After the reductive annealing treatment, additional signals of metallic Ni0 were detected, and their intensities increase with increasing annealing temperature. Similarly, the W 4f spectra of the reduced samples clearly manifested the formation of W(IV) and W0 species upon reduction. These results were in accord with XRD, SAED, and HRTEM observations, supporting the evolutionary formation of Ni–W alloys and W-containing substrate phases during the reduction process. A close examination of the XPS spectra further found subtle but significant binding energy shifts of Ni0 and W0. Specifically, the BEs of Ni0 in the reduced samples were observed to negatively shift in comparison with the BE of pristine metal Ni at 853.3 eV. Meanwhile, the W0 in the reduced samples showed positive BE shifts relative to pure W (31.0 eV). These results clearly indicated the electron transfer from W to Ni as a consequence of Ni–W alloys formation. In addition, XPS analysis clearly detected Ni(II) and W(VI) signals throughout the reduced samples but with decreased intensities upon high-temperature annealing. These results, together with the XRD, Raman, and HRTEM characterizations **(Figure 6a, and 6b**), suggested the presence of $NiWO_4$ and WO_{3-x} amorphous phases in the reduced samples. On the basis of the combination of phase, microstructure, and chemical state analyses, the resulting nanocatalysts from reductive annealing of the $NiWO_4$ precursor at different temperatures were denoted as $Ni_{17}W_3/NiWO_4$ (350°C), $Ni_4W/WO_2/NiWO_4$ (400°C), and $Ni_4W/W/WO_{3-x}$ (600 °C), respectively

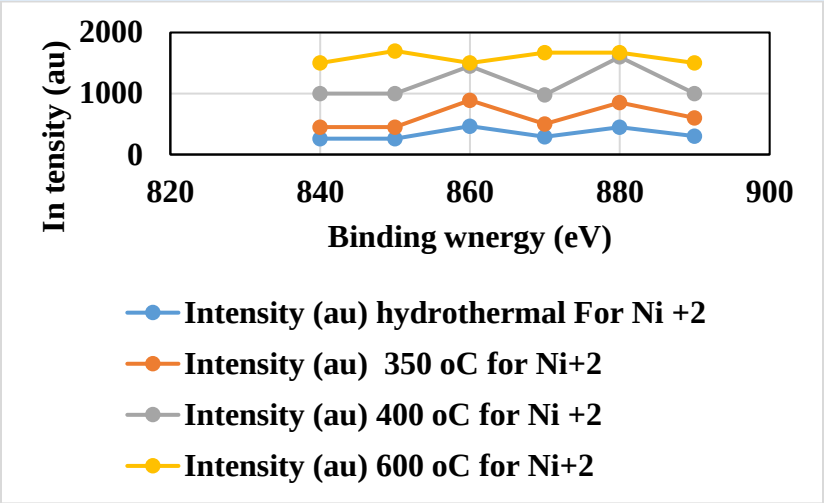

Figure 6a: XPS analysis in Ni^{+2} samples

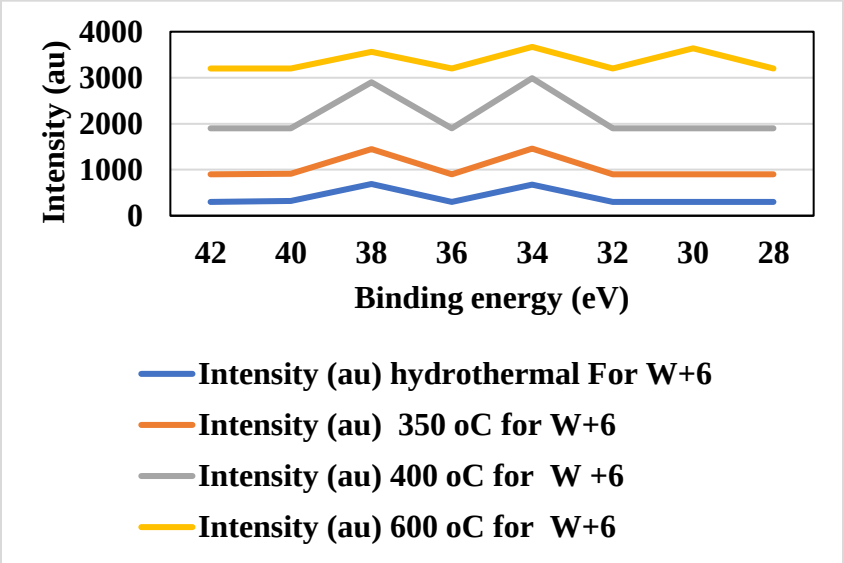

Figure 6b: XPS spectra in W^{+6} samples

1.13.Photodegration pathway

Previous studies illustrated that different initial adsorption conformations of N_2H_4 over metal surfaces can lead to distinct reaction pathways. In the case of only one N atom of N_2H_4 bonded to the metal surfaces, N–H bond cleavage of N_2H_4 molecules is energetically more favorable than N–N bond cleavage, which preferably results in H_2(g) production. In contrast, the adsorption conformation with both N atoms of N_2H_4 bonding to the surfaces dominantly leads to NH_3 formation. Hence, the adsorption energy difference between one-N-atom and two-N-atom conformations can serve as an indicator to evaluate the reaction selectivity of N_2H_4 decomposition. According to the DFT calculation results, the adsorption energy difference on the Ni_4W surface is larger than that on the $Ni_{17}W_3$ surface by nearly a factor of 2, implying a significantly higher H_2(g) selectivity for Ni_4W. This is in good accordance with the experimental results. Therefore, it can be concluded that the improved catalytic performance of the Ni–W–O-derived catalysts upon increasing the annealing temperature from 350 to 400°C should stem from the resultant Ni_4W with higher intrinsic activity and H_2(g) selectivity than $Ni_{17}W_3$. The reaction rate of the system rapidly reached its maximum [90 ml (N_2 + H_2) min^{-1}] within ~1 min and maintained at a level of ~80 ml (N_2 + H_2) min^{-1} for over 80 min (**Figure 7**).

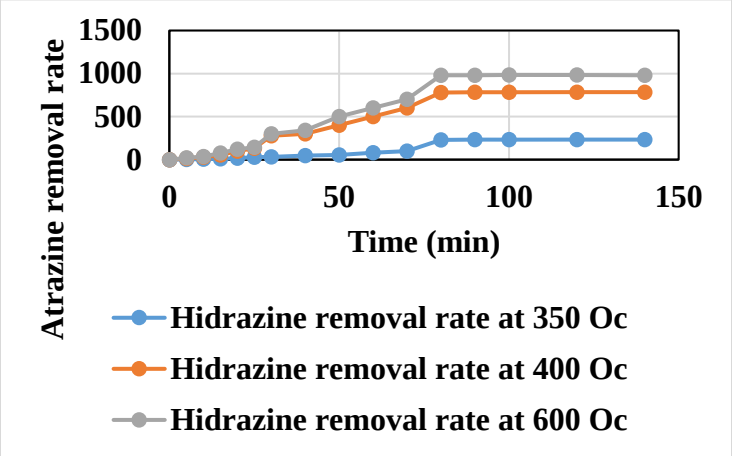

Figure 7: Photodegradation kinetic of hydrazine

Conclusions

The Ni–W–O-derived nanocomposite catalysts can be readily synthesized under laboratory conditions. The prepared catalysts exhibited remarkably distinct catalytic performances toward $N_2H_4.H_2O$ decomposition regarding H_2(g) production. Using this noble-metal-free catalyst, decomposition of $N_2H_4.H_2O$ to hydrogen production was performed. For maximum photodegradation of hydrazine monohydrate to H_2(g) the optimum operatinal conditions can be summarized as follws: Ni–W–O nanocomposite concentration of 2 mg/l with a Ni/W/O ratio of 0.8 / 0.5 / 0.2, 80 min irradiation time, a ligth power of 90 W/m^2, a temperature of 60^{o}C and a pH of 8.0. XRD, FTIR patterns, TEM images and UV−vis spectra of the catalyst exhibited the performances of noble-metal-free catalysts to produce efficiently H_2(g) from $N_2H_4.H_2O$. With this nanocomposite catalyst may produce H_2(g) as fuel source.

Acknowledgement

This research study was undertaken in the Environmental Microbiology Laboratories at Dokuz Eylül University Engineering Faculty Environmental Engineering Department, Izmir, Turkey. The authors would like to thank this body for providing financial support.

References

1. Schlapbach, L., Züttel, A.(1992). Hydrogen-storage materials for mobile applications. Nature, 2001;414 (6861):353-358.
2. Sandrock, G., Suda, S., Schlapbach, L. Hydrogen in intermetallic compounds II. Top. Appl. Phys.67(5):197-258.
3. Orimo S.-I., Nakamori, Y., Eliseo, J.R, Andreas Züttel, A., Jensen, C.M. (2007). Complex hydrides for hydrogen storage. Chem. Rev.,107(10):4111-4132.
4. Suh MP; Park HJ; Prasad TK; et al.(2012). Hydrogen storage in metal-organic frameworks. Chem. Rev.112(2):782-835.
5. Hirscher, M., Autrey, T., Orimo, S.I(.2009). Hydrogen energy. ChemPhysChem, 20(10):1157-1157.
6. Dagdougui, H., Sacile, R., Bersani, C., Ouammi, A. (2008). Hydrogen infrastructure for energy applications: Implementation scenarios. Chapter 4, Academic Press, 3752.
7. Preuster, P., Alekseev, A., Wasserscheid, P. (2017). Hydrogen storage technologies for future energy systems. Annu. Rev. Chem. Biomol. Eng.,8:445-471.
8. Yartys, V.A., Lototskyy, M.V., Akiba, E., Albert, R., Antonov, V.E., Ares, J.R., Baricco, M., Bourgeois, N., Buckley, C.E., Bellosta von Colbe, J.M., Crivello, J.-C., Cuevas, F., Denys, R.V., Dornheim, M., Felderhoff, M., Grant, D.M., Hauback, B.C., Humphries, T.D., Jacob, I., Jensen, T.R., de Jongh, P.E., Joubert, J.-M., Kuzovnikov, M.A., Latroche, M., Paskevicius, M., Pasquini, L., Popilevsky, L., Skripnyuk, V.M., Rabkin, E., Sofianos, M.V., Stuart, A., Walker, G., Wang, H., Webb, J.C., Zhu, (2019). M. Magnesium based materials for hydrogen based energy storage: past, present and future. Int. J. Hydrogen Energy, 44(15):7809-7859.
9. Milanese, C., Jensen, T.R., Hauback, B.C., Pistidda, C., Dornheim, M., Yang, H., Lombardo, L., Zuettel, A., Filinchuk, Y., Ngene, P., de Jongh, P.E., Buckley, C.E., Dematteis, E.M., Baricco, M.(2019). Complex hydrides for energy storage. Int. J. Hydrogen Energy, 44:7860-7874.
10. Paskevicius, M., Jepsen, L.H., Schouwink, P., Černý, R., Ravnsbæk, D.B., Filinchuk, Y., Dornheim, M., Besenbacherf, F., Jensen, T.R. (2017). Metal borohydrides and derivatives–synthesis, structure and properties. Chem. Soc. Rev., 46(5):1565-1634.
11. Kumar, R., Karkamkar, A., Bowden, M., Autreya, T. (2019). Solid-state hydrogen rich boron–nitrogen compounds for energy storage. Chem. Soc. Rev 48 (21), 5350-5380.
12. Hansen, B.R.S., Paskevicius, M., Li, H.W., Akiba, E., Jensen, T.R. (2016). Metal boranes: Progress and applications. Coord. Chem. Rev., 323(15):60-70.
13. Møller, K.T., Sheppard, D., Ravnsbæk, D.B., Buckley, C.E., Akiba, E., Li, H.-W., Jensen, T.R. (2017). Complex metal hydrides for hydrogen, thermal and electrochemical energy storage. Energies, 10(10):1645-1675.
14. Zhu, Q.L., Xu, Q. (2015). Liquid organic and inorganic chemical hydrides for high-capacity hydrogen storage. Energy Environ. Sci.8(2):478-512.
15. Demirci, U.B., Miele, P. (2011). Chemical hydrogen storage: 'material' gravimetric capacity versus 'system' gravimetric capacity. Energy Environ. Sci.,4(9):3334-3341.
16. Schmidt, E.W. Hydrazine and its derivatives. Preparation, properties, applications, 2nd ed.; John Wiley & Sons: New York, 2001.
17. Yadav, M., Xu, Q.(2012). Liquid-phase chemical hydrogen storage materials. Energy Environ. Sci.,5(12):9698-9725.
18. Cho, S.J., Lee, J., Lee, Y.S., Kim, D.P. Characterization of iridium catalyst for decomposition of hydrazine hydrate for hydrogen generation. Catal. Lett., 2006;109(3–4):181-186.
19. Singh, S.K., Zhang, X.B., Xu, Q. (2009). Room-temperature hydrogen generation from hydrous hydrazine for chemical hydrogen storage. J. Am. Chem. Soc., 131(20):9894-9895.
20. Singh, S.K., Xu, Q. (2009). Complete conversion of hydrous hydrazine to hydrogen at room temperature for chemical hydrogen storage. J. Am. Chem. Soc., 131(50):18032-18033.

21. Singh, A.K., Yadav, M., Aranishi, K., Xu, Q. (2012). Temperature-induced selectivity enhancement in hydrogen generation from Rh-Ni nanoparticle-catalyzed decomposition of hydrous hydrazine. Int. J. Hydrogen Energy 37(24):18915-18919.
22. Singh, S.K., Xu, Q. (2010). Bimetallic Ni-Pt nanocatalysts for selective decomposition of hydrazine in aqueous solution to hydrogen at room temperature for chemical hydrogen Storage. Inorg. Chem., 49(13):6148-6152.
23. Singh, S.K., Iizuka, Y., Xu, Q. (2011). Nickel-palladium nanoparticle catalyzed hydrogen generation from hydrous hydrazine for chemical hydrogen storage. Int. J. Hydrogen Energy., 36(18):11794-11801.
24. Singh, S.K., Xu, Q. (2010). Bimetallic nickel-iridium nanocatalysts for hydrogen generation by decomposition of hydrous hydrazine. Chem. Commun.,46(35):6545-6547.
25. Singh, S.K., Singh, A.K., Aranishi, K., Xu, Q. Noble-metal-free bimetallic nanoparticle-catalyzed selective hydrogen generation from hydrous hydrazine forchemical hydrogen storage. J. Am. Chem. Soc., 2011;133(49):19638–19641.
26. He, L., Huang, Y., Wang, A., Wang, X., Chen, X., Delgado, J.J., Zhang, T. (2012). A noble-metal-free catalyst derived from Ni-Al hydrotalcite for hydrogen generation from $N_2H_4.H_2O$ decomposition. Angew. Chem., Int. Ed.;51(25):6191–6194.
27. Dai, H., Zhong, Y., Wang, P.(2017). Hydrogen generation from decomposition of hydrous hydrazine over Ni-Ir/CeO_2 catalyst. Prog. Nat. Sci., 27(1):121-125.

DOI:10.31579/2693-4779/158